Research Article Vol. 31, No. 16 / 31 Jul 2023 / Optics Express 25993

Optics EXPRESS

# Three-dimensional echo light field analysis for dual-band laser active detection of a cat-eye optical system

ZHE LV,[1,2] KUO ZHANG,[1,*] RUI BAO,[1,2] HANG ZHOU,[3] KE YANG,[3] WEIWEI LI,[1,2] XINCHEN DU,[1,2] AND FEI CHEN[1]

[1] *Changchun Institute of Optics, Fine Mechanics and Physics, Chinese Academy of Sciences, Changchun 130033, China*
[2] *University of Chinese Academy of Sciences, Beijing 100049, China*
[3] *Laboratory of Electromagnetic Space Cognition and Intelligent Control, Beijing 100049, China*
[*] *zhangkuo_fx@163.com*

**Abstract:** Laser active detection technology utilizing the cat-eye effect provides rapid response, precise positioning, and long detection distances. However, current research mainly focuses on active detection within a single visible or near-infrared band, lacking quantitative analyses of the echo spot. In this paper, a four-interval theoretical model for dual band cat-eye target echo detection was constructed using matrix optics theory and Collins diffraction integration method. Dual-band echo detection experiments were conducted using 10.6 um far-infrared waves and 532 nm visible light waves, also the power, radius, and target-missing quantities of the echo spots were collected and quantitatively compared with the theoretical results. Results indicate that, due to the diffraction limit's effect on the distribution of the echo field, the echo power of far-infrared band detection is smaller than that of visible light band detection. The impact on the light spot caused by the positive and negative defocus values is asymmetric, with positive defocus having a lower impact on the echo spot than negative defocus at the same value. A weak positive defocus value that minimizes the radius of the echo spot and maximizes the echo power exists, with the value of weak positive defocus varying between detection bands. A linear relationship exists between the incident angle of the detection laser and the deviation of the echo spot. These findings provide a foundation for extracting working band details, predicting the motion trajectory of moving cat-eye targets, and achieving real-time tracking and detection recognition during laser active detection.



## 1. Introduction

Most optoelectronic devices designed for imaging and detection currently rely on the use of specific aperture optical systems to collect and focus light signals onto photodetectors. Therefore, when a laser beam that is actively detecting a target enters the field of view of the target's optical system, the reflected beam from the detector will travel back along the original path (known as the cat-eye effect principle [1]) thanks to the reversibility of the optical path. The cat-eye optical system collimates the detecting laser, causing the reflected light intensity to be 2 to 4 orders of magnitude greater than general diffuse reflection. This characteristic of the cat-eye optical system makes laser active detection technology utilizing the cat- eye effect a promising method for achieving remote target detection and high-precision localization [2].

Since the 1980s, several countries, including the United States, Great Britain, and Russia, have developed a range of portable, vehicle-mounted, airborne, and ship-borne laser weapons systems utilizing the cat eye effect [3–6]. Laser active detection technology based on the cat eye effect has found rapid application on the battlefield due to its superior sensitivity, responsiveness, and accuracy compared to passive detection technology. Furthermore, it can be easily combined

#494618 https://doi.org/10.1364/OE.494618
Journal © 2023 Received 9 May 2023; revised 10 Jun 2023; accepted 10 Jun 2023; published 20 Jul 2023

Optics EXPRESS

with various laser weapons and infrared directional countermeasure systems to enhance combat effectiveness. In recent years, researchers mainly use geometrical optics ray tracing method and physical optics simulation method to study the echo beam characteristics of cat's eye optical system. The ray tracing method of geometrical optics has a large error in calculating the far-field propagation and passing through a finite aperture, so it is impossible to get an accurate description of the far-field light field. The physical optics simulation method lacks quantitative analysis of the impact of variables such as angle and defocus on the echo spot, and lacks simulation of three-dimensional echo images [7,8]. He et al. proposed trajectory prediction algorithms to address difficulties in achieving real-time detection of low-speed moving cat-eye targets [9,10]. Lv et al. proposed a multi-band cat-eye target echo light field distribution model by incorporating the focal length of the dispersion lens into the matrix optical transmission process [11]. Zhao et al. proposed the use of the Collins diffraction integral formula to obtain the analytical formula of the echo beam distribution of a cat-eye optical system [12]. Wu et al. introduced the concepts of the optical transmission matrix and combined diffraction aperture to obtain a further cat-eye target echo light field model.

With the rapid development of intelligent and multifunctional optoelectronic devices, the range of wavelengths used is becoming increasingly diverse and gradually shifting to the far-infrared band [13,14]. Therefore, it is necessary to analyze the impact of different bands, especially the far-infrared band, on the echo spot of optoelectronic devices and to efficiently and accurately collect important information such as the working band and target position. However, most of the laser active detection technology based on the cat-eye effect currently focuses on the detection of a single wavelength in the visible and near-infrared bands, with little research reported on the far-infrared band detection. In addition, there is a lack of quantitative analysis of the effects of variables such as incident wavelength, defocus amount and incident angle on the echo spot in terms of both experimental and theoretical aspects. To construct a more efficient and accurate model for detecting targets utilizing both visible and far-infrared bands, this paper proposes to develop a four-interval theoretical model for dual-band cat-eye target echo detection. Moreover, the paper will conduct a detailed quantitative analysis of the impacts of various variables on the echo spot, including incident wavelength, defocus amount, and incident angle. Corresponding dual-band echo spot detection experiments and theoretical results are compared and analyzed. Echo spot images are collected from experimental and theoretical results, and corresponding data such as echo power, echo spot radius, centroid position, and centroid target-missing quantities amount are extracted to quantitatively study the echo spot and its influencing factors. The theoretical and experimental results of this paper can provide a theoretical basis for extracting working band information of cat-eye targets and predicting the trajectory of moving cat-eye targets in laser active detection, thus achieving real-time tracking and detection recognition.

This paper is organized as follows. In Section 2, we construct a four-interval theoretical model for detecting dual-band cat-eye targets. In Section 3, we introduced the specific experimental setup and steps for dual band echo spot detection. In Section 4, we compared and discussed the theoretical model and experimental results of echo spot detection. We conclude our discussion in Section 5.

## 2. Theoretical model

This paper proposes a theoretical deduction of the three-dimensional echo light field distribution of dual-band cat-eye targets using matrix optics theory and the Collins diffraction integral formula with an aperture function expansion in the sum of complex Gauss functions. The cat-eye target consists of a focusing lens and a flat mirror as depicted in Fig. 1. The process of detecting an incident laser on the cat-eye target and returning it to the receiving plane is symmetrical, allowing it to be transformed into a transmission optical path for processing. At this point, lens 2 is symmetrically unfolded for lens 1, and the changes that occur between the two lenses will be the same, such as the subsequent rotation angle being the same. However, the model proposed by Wu did not consider the defocusing effect of the detector on the cat-eye target's photosensitive surface [15–17]. Therefore, this paper divides the intermediate optical interval into two parts, evolving from a three-interval model to a four-interval model for research deduction. The four interval model proposed in this article has two advantages over the current three interval model: firstly, it includes the defocusing variable of the detector on the photosensitive surface of the cat-eye target in the formula derivation; secondly, it can introduce wavelength variables into the three-dimensional echo spot distribution.

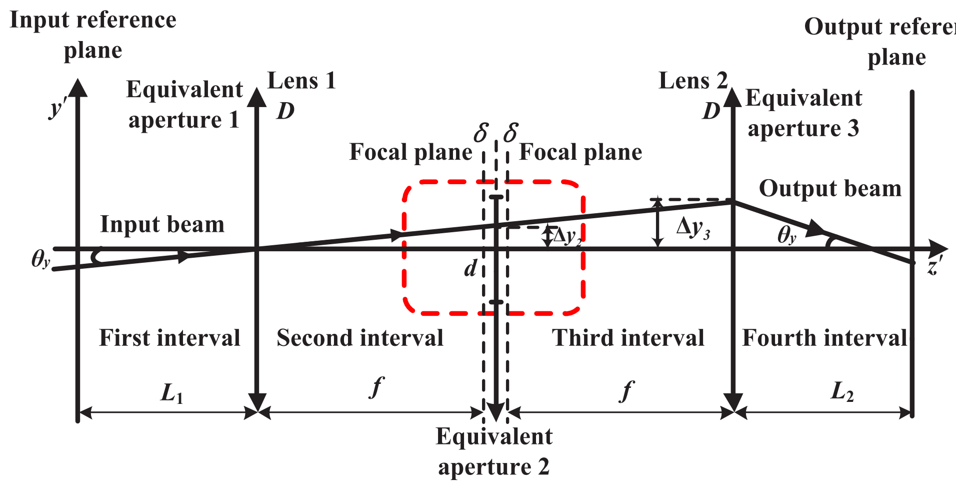


**Fig. 1.** Cat-eye effect reflection model diagram.

Figure 1 illustrates the incident angle of the detection laser, denoted as $\theta_y$, entering the cat-eye target. When the laser reaches the photosensitive surface of the target, the change in incident angle initiates a displacement change, represented by $\Delta y_2$. Similarly, when the laser returns to the lens of the target, the change in incident angle generates a displacement change $\Delta y_3$. Notably, the application of Collins diffraction integral formula is restricted to small angles and paraxial transmission. However, in laser active detection practices, it is rare to observe the incidence of the cat-eye target perpendicular to the detection direction. Thus, this study adopts a method by rotating the coordinate axis to analyze the displacement change $\Delta y$ due to angle variation instead of the incident angle $\theta_y$. In Fig. 1, the coordinate system is $x'y'z'$, where the z' axis denotes the direction of the cat-eye optical system axis. Subsequently, Fig. 2 depicts the rotation of the coordinate axis in the direction of the incident light establishment of a new coordinate system-$xyz$, where the z-axis represents the direction of the incident light. Consequently, the change in incident angle $\theta_y$ at the optical axis is converted to a displacement change $\Delta y$. The conversion formula is shown in Formula 1. Moreover, the equivalent aperture of the photosensitive surface of the cat-eye target converts from a circular aperture with a hard edge to an elliptical aperture, and the displacement change is represented by the coordinate value of the elliptical center, meaning $\Delta y_2$.

$$\begin{aligned} \Delta x_2 &= -f \cdot \tan\theta_x, \Delta y_2 = -f \cdot \tan\theta_y \\ \Delta x_3 &= -2f \cdot \tan\theta_x, \Delta y_3 = -2f \cdot \tan\theta_y \end{aligned} \tag{1}$$

where $\theta x$ and $\theta y$ are the oblique angles of the incident laser in the $x$ and $y$ directions, respectively, and $\Delta x$ and $\Delta y$ are the vertical distances between the centre of the equivalent diaphragm and the new $z$-axis after the rotation of the coordinate axis in the $x$ and $y$ directions, respectively.

Optics EXPRESS

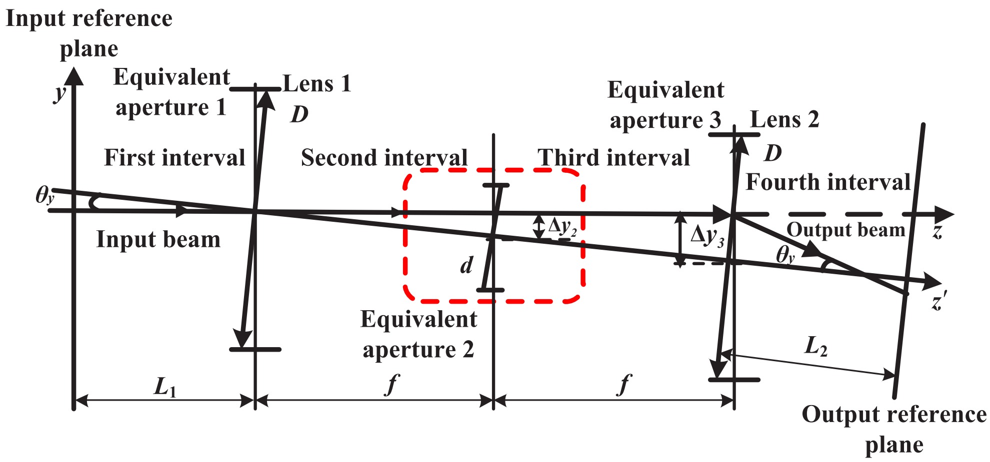


**Fig. 2.** Cat-eye effect reflection model diagram after coordinate rotation.

As the emitting beam tilts into the cat-eye target, the shapes of the three equivalent hard-edge apertures become elliptical after the rotation of the coordinate axis. Therefore, the window functions of the three equivalent apertures can be expressed as follows:

$$M_1(x_1,y_1)=\begin{cases}1, \frac{x_1^2}{\cos^2\theta_x}+\frac{y_1^2}{\cos^2\theta_y}\leqslant\left(\frac{D}{2}\right)^2\\ 0, \text{otherwise}\end{cases}$$
$$M_2(x_2,y_2)=\begin{cases}1, \frac{(x_2-\Delta x_2)}{\cos^2\theta_x}+\frac{(y_2-\Delta y_2)}{\cos^2\theta_y}\leqslant\left(\frac{d}{2}\right)^2\\ 0, \text{otherwise}\end{cases} \tag{2}$$
$$M_3(x_3,y_3)=\begin{cases}1, \frac{(x_3-\Delta x_3)}{\cos^2\theta_x}+\frac{(y_3-\Delta y_3)}{\cos^2\theta_y}\leqslant\left(\frac{D}{2}\right)^2\\ 0, \text{otherwise}\end{cases}$$

Figure 2 depicts the four matrix optical interval, with the first interval spanning from the input reference surface to the front mirror surface of lens 1, without the presence of a hard-edged aperture. The corresponding transmission matrix is expressed as follows:

$$\begin{bmatrix} a_1 & b_1 \\ c_1 & d_1 \end{bmatrix}=\begin{bmatrix} 1 & L_1 \\ 0 & 1 \end{bmatrix}, \tag{3}$$

where $L_1$ is the detection distance from the input reference surface to the cat-eye lens.

The second optical interval extends from the front mirror surface of lens 1 to the front plane of the detector, and it incorporates lens 1's hard-edged aperture (with a diameter of $D$). In this interval, the dispersion relationship of the lens introduces two variables, namely wavelength and defocus. The corresponding transmission matrix is expressed as follows:

$$\begin{bmatrix} a_2 & b_2 \\ c_2 & d_2 \end{bmatrix}=\begin{bmatrix} 1 & f_0+\delta \\ 0 & 1 \end{bmatrix}\begin{bmatrix} 1 & 0 \\ -\frac{1}{f(\lambda)} & 1 \end{bmatrix}=\begin{bmatrix} 1-\frac{f_0+\delta}{f(\lambda)} & f_0+\delta \\ -\frac{1}{f(\lambda)} & 1 \end{bmatrix}$$
$$f(\lambda)=f_0\cdot\frac{n_0-1}{n(\lambda)-1}, \tag{4}$$

where $f_0$ and $n_0$ are the lens focal length and lens refractive index corresponding to the central wavelength of the cat-eye target, respectively, $\delta$ is the off-focus of the cat-eye target, and $f(\lambda)$

and $n(\lambda)$ are the focal length and refractive index of the cat-eye target lens corresponding to the incident laser wavelength, respectively.

The third optical interval extends from the front plane of the detector to the front mirror surface of lens 2, and it incorporates detector's hard-edged aperture (with a diameter of $d$). The corresponding transmission matrix is expressed as follows:

$$\begin{bmatrix} a_3 & b_3 \\ c_3 & d_3 \end{bmatrix} = \begin{bmatrix} 1 & 0 \\ -\frac{1}{f(\lambda)} & 1 \end{bmatrix} \begin{bmatrix} 1 & f_0+\delta \\ 0 & 1 \end{bmatrix} = \begin{bmatrix} 1 & f_0+\delta \\ -\frac{1}{f(\lambda)} & 1-\frac{f_0+\delta}{f(\lambda)} \end{bmatrix}. \tag{5}$$

The fourth optical interval extends from the front mirror surface of lens 2 to the output reference surface, and it incorporates lens 2's hard-edged aperture (with a diameter of $D$). The corresponding transmission matrix is expressed as follows:

$$\begin{bmatrix} a_4 & b_4 \\ c_4 & d_4 \end{bmatrix} = \begin{bmatrix} 1 & L_2 \\ 0 & 1 \end{bmatrix}, \tag{6}$$

where $L_2$ is the detection distance from the output reference surface to the detection plane.

Using the Collins diffraction integral formula, the optical field distribution of the emitted beam passing through the first interval to the front mirror of lens 1 can be deduced as follows:

$$\begin{aligned} E_1(x_1,y_1) = {} & \frac{i}{\lambda b_1} \cdot \exp(ikL_1) \cdot \iint_{-\infty}^{\infty} E_0(x_0,y_0) \cdot \\ & \exp\left\{-\frac{ik}{2b_1}\left[a_1\left(x_0^2+y_0^2\right) - 2(x_0x_1+y_0y_1) + d_1\left(x_1^2+y_1^2\right)\right]\right\} \mathrm{d}x_1\mathrm{d}y_1. \end{aligned} \tag{7}$$

Using the special integral formula, the above equation can be expressed as:

$$E_1(x_1,y_1) = \frac{ik}{2b_1P_1^2} \cdot \exp(ikL_1) \cdot \exp\left[-\left(\frac{ikd_1}{2b_1} + \frac{k^2}{4b_1^2P_1^2}\right) \cdot (x_1^2+y_1^2)\right], \tag{8}$$

where,

$$k = \frac{2\pi}{\lambda}, P_1^2 = \frac{1}{w_0^2} + ik\frac{a_1}{2b_1}. \tag{9}$$

The derivation process for the transmission beam through the second, third, and fourth interval is comparable to that of the first interval. I have previously detailed this theoretical derivation process in Ref. [13]. Therefore, I will not elaborate on it further in this paper. The final derivation results in the light field distribution of the transmission beam arriving at the output reference surface after passing through each region, which is indicated as follows:

$$\begin{aligned} E_4(x_4,y_4) = {} & \frac{ik}{2b_1P_1^2}\frac{ik}{2b_2}\frac{ik}{2b_3}\frac{ik}{2b_4}\exp[ik(L_1+L_2+2f)]\exp\left[-\frac{ikd_4}{2b_4}\left(x_4^2+y_4^2\right)\right]\sum_{j_1=1}^{M}\frac{F_{j_1}}{P_{2x}P_{2y}} \\ & \cdot\sum_{j_2=1}^{M}\frac{F_{j_2}}{P_{3x}P_{3y}}\exp\left[\frac{16G_{j_2}^2}{d^4}\left(\frac{\Delta x_2^2}{P_{3x}^2\cos^4\theta_x} + \frac{\Delta y_2^2}{P_{3y}^2\cos^4\theta_y}\right)\right]\exp\left[-\frac{4G_{j_2}}{d^2}\cdot\left(\frac{\Delta x_2^2}{\cos^2\theta_x} + \frac{\Delta y_2^2}{\cos^2\theta_y}\right)\right] \cdot \\ & \sum_{j_3=1}^{M}\frac{F_{j_3}}{P_{4x}P_{4y}}\exp\left[-\frac{k^2}{4b_4^2P_{4x}^2}\left(x_4 - \frac{8ib_4G_{j_3}\Delta x_3}{kD^2\cos^2\theta_x} + \frac{4b_4G_{j_2}\Delta x_2}{b_3P_{3x}^2d^2\cos^2\theta_x}\right)^2\right] \cdot \\ & \exp\left[-\frac{k^2}{4b_4^2P_{4y}^2}\left(y_4 - \frac{8ib_4G_{j_3}\Delta y_3}{kD^2\cos^2\theta_y} + \frac{4b_4G_{j_2}\Delta y_2}{b_3P_{3y}^2d^2\cos^2\theta_y}\right)^2\right]\exp\left[-\frac{4G_{j_3}}{D^2}\left(\frac{\Delta x_3^2}{\cos^2\theta_x} + \frac{\Delta y_3^2}{\cos^2\theta_y}\right)\right] \end{aligned} \tag{10}$$

Optics EXPRESS

where,

$$\begin{aligned} P_{4x}^2 &= \frac{ika_4}{2b_4} + \frac{ikd_3}{2b_3} + \frac{k^2}{4b_3^2P_{3x}^2} + \frac{4G_{j_3}}{D^2\cos^2\theta_x} \\ P_{4y}^2 &= \frac{ika_4}{2b_4} + \frac{ikd_3}{2b_3} + \frac{k^2}{4b_3^2P_{3y}^2} + \frac{4G_{j_3}}{D^2\cos^2\theta_y} \end{aligned}. \tag{11}$$

Therefore, the light intensity distribution at the output reference plane can be written as:

$$I_4(x_4, y_4) = E_4(x_4, y_4) \cdot E_4^*(x_4, y_4). \tag{12}$$

## 3. Experimental setup

This paper utilizes a controlled variable methodology to perform a three-dimensional echo field detection experiment on bi-band cat-eye targets. The bi-band consists of visible light and far-infrared, with detection performed at distances of 18 m. The primary objective of this study is to investigate the effects of three variables: incident wavelength, incident detection laser angle, and defocus amount on the three-dimensional echo field of the cat-eye target. The specific parameters of the emission laser in the two band experiments are shown in Table 1.

**Table 1. The parameters of the emission laser in the two band experiments**

| Emission laser parameters | Visible laser | Far-infrared laser |
|---|---|---|
| Emission wavelength | 532 nm | 10.6 um |
| Transmitting power | 0-2 W | 0-15 W |
| Power stability (rms, over 4 hours) | < 1% | < 3% |
| Spectral linewidth | < 0.1 nm | < 1.4 um |
| Beam divergence, full angle | < 1.2 mrad | < 3.0 mrad |
| Spot diameter | 4 mm | 2 mm |

### *3.1. Cat-eye target echo field detection experiment in the 532 nm wavelength*

This study utilizes an experimental design employing a coaxial transmitting and receiving system to accurately collect detailed data regarding the echo field distribution under varied conditions. Figure 3 depicts the three-dimensional echo field detection optical path for the cat-eye target in the 532 nm wavelength. N-BK7 was utilized to construct all lenses in the experiment, while the main optical system was a polarized beam splitter (PBS) system. This optical system achieved the separation of reflection and reception optical paths while ensuring coaxial alignment of both systems. The imaging optical system that followed further facilitated the receipt and processing of the signals. The collimation, focusing, and expansion of the Gaussian beam were achieved through the utilization of a conjugate telescope system, composed of a double cemented negative lens ($L_1$) with $f_1$ = -50 mm and a double cemented achromatic lens ($L_2$) with $f_2$ = 200 mm. The laser beam in the experiment was converted into P-polarized light parallel to the incident surface using an optical polarizer (OP). It then passed through the polarized beam splitter and finally arrived at the cat-eye target. The reflected beam from the cat-eye lens reflection surface passed through a quarter wave plate (QWP) and then, after two passes through another quarter wave plate, P-polarized light became S-polarized light vibrating vertically to the incident surface, reflecting it at the receiving plane. Finally, the diffracted light spots produced in the experiment were received by a beam quality analyzer and a power meter located at the side of the polarized beam splitter.

The experimental set up underlying Fig. 3 employed a common set of telescope systems in both the laser transmitting and receiving systems. The use of a telescope system in the transmitter

Optics EXPRESS

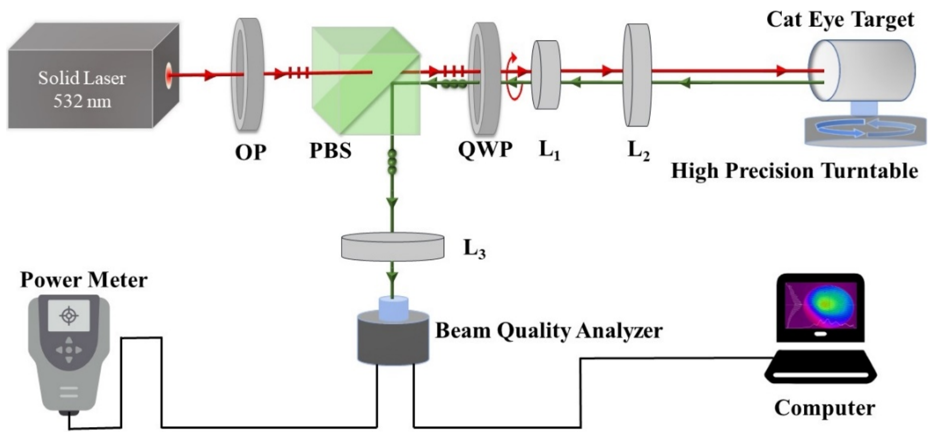


**Fig. 3.** Experimental schematic diagram of three-dimensional echo light field detection optical path for cat-eye targets in the 532 nm wavelength.

path resulted in the expansion of the laser spot. This expansion was useful in ensuring a complete entrance of the probing beam into the cat-eye target. The use of the telescope system in the receiver path facilitated the collection of additional diffraction pattern information in the beam quality analyzer. The telescope system used in the experiment featured respective focal lengths of -50 mm and 200 mm. To maximize the collection of diffraction patterns, the laser beam was expanded four times, and a lens with a larger radius was selected.

The physical layout of the optical path is presented in Fig. 4. Figure 4(a) depicts the layout of the transmitting and receiving ends, while Fig. 4(b) displays the 532 nm wavelength cat-eye target and high-precision turntable. The laser emission source had a wavelength of 532 nm, an adjustable power range of 0 to 2.5 W. The cat-eye target comprised a focusing lens with a focal length of 50 mm and a silicon plane window mirror. During the system adjustment process, the quarter wave plate angle was altered to mitigate the influence of reflected light from the lenses on the received diffraction pattern. The optical polarizer was adjusted to enable only P-polarized light vibrating parallel to the incident surface to transmit, ensuring the greatest transmitted light intensity. The distance between the double cemented negative lens $L_1$ and the double cemented achromatic lens $L_2$ was adjusted to achieve a parallel laser beam output, ensuring the beam exited collimated. The conjugate telescope system was then calibrated to produce a laser beam that was parallel and fully covered the cat-eye target lens. The system and the target position were further adjusted to maximize reflection at the receiver end, resulting in a circular reflected spot on the beam quality analyzer. The incident angle of 0° was recorded.

### *3.2. Cat-eye target echo field detection experiment in the 10.6 um wavelength*

The procedure employed to detect the three-dimensional echo optical field of the cat-eye target in the 10.6 um wavelength was similar to that utilized for the 532 nm wavelength procedure. However, given the invisibility of the far-infrared band, an additional indicator optical path was necessary to achieve convergence. In order to achieve this, specific optical path principles were applied, as depicted in Fig. 5. The lenses employed in the 10.6 um wavelength experiment were fabricated from ZnSe. A thin-film polarizer (TFP) system was used to achieve the same splitting action as the PBS system in the 532 nm wavelength, when the laser incidence angle was 67.4°, separating the reflection and reception optical paths. The use of a conjugate telescope system, consisting of a concave lens ($L_1$) with $f_1 = -50$ mm and a convex lens ($L_2$) with $f_2 = 200$ mm, enabled the collimation, focusing, and expansion of the Gaussian beam. The conjugate

Optics EXPRESS

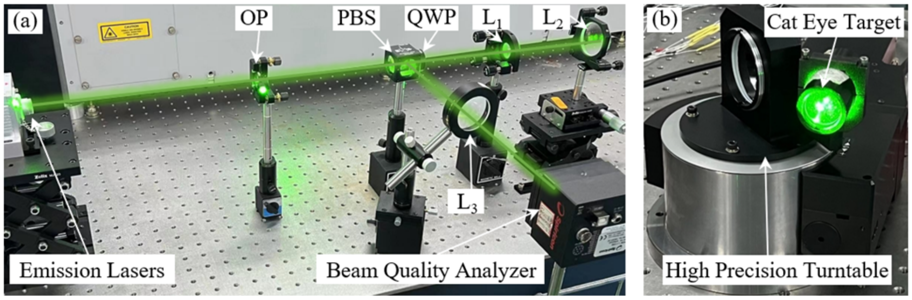


**Fig. 4.** (a) Physical image of the optical path of the transmitter and receiver for detecting the cat-eye target echo light field in the 532 nm wavelength. (b) Physical image of cat-eye target in the 532 nm wavelength and high precision turntable.

telescope system's significance, as used in the 532 nm wavelength experiment, is the same in this application.

The experiment employed 10.6 um wavelength light as the probing laser and 532 nm light as the indicator laser. Initially, both light beams traversed a high-transmittance high-reflectance mirror (HTHRM), with the 10.6 um beam fully transmitting and the 532 nm beam fully reflecting. A continuous adjustment of the mirror angle aligned the two light beams perfectly, at both short and long distances, enabling beam coupling. The transmitted P-polarized light that was parallel to the incident plane in the incident beam was entirely reflected after traversing through the far-infrared thin-film polarizer at a 45° angle and accessing the far-infrared reflective quarter-wave plate (RPR), before reaching the cat-eye target through a conjugate telescope system. The reflected beam from the cat-eye lens surface again passed through the far-infrared reflective quarter-wave plate. After passing twice through the quarter-wave plate, the P-polarized light converted to S-polarized light, which is perpendicular to the incident plane and eventually reflected onto the receiving plane. After locating the incident light spot's position, the indicator light was disabled during the experiment. The diffraction light spot obtained was analyzed using a 10.6 um wavelength beam quality analyzer and a power meter located at the rear of the far-infrared thin-film polarizer.

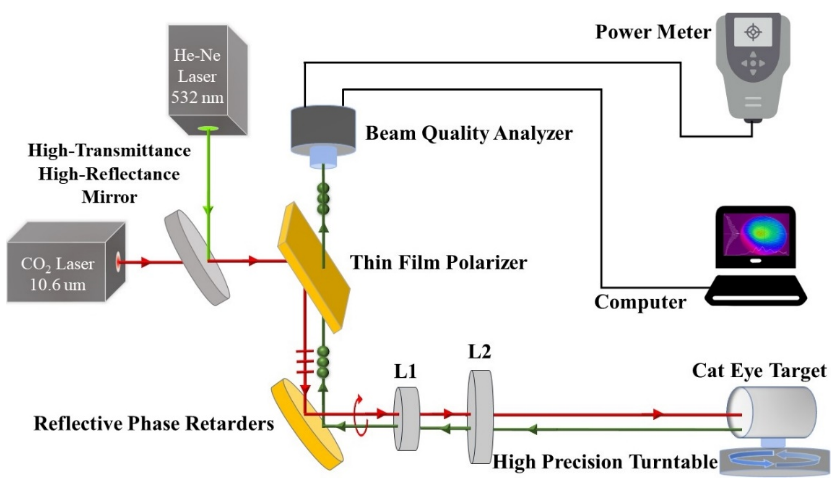


**Fig. 5.** Experimental schematic diagram of three-dimensional echo light field detection optical path for cat-eye targets in the 10.6 um wavelength.

Figure 6 illustrates the physical diagram of the experimental optical path. Figure 6(a) depicts the optical path for the transmitting and receiving ends, while Fig. 6(b) presents the 10.6 um wavelength cat-eye target and high-precision rotary table. The transmitting laser was characterized by a wavelength of 10.6 um and adjustable power ranging from 0 to 20 W. The cat-eye target consisted of a focusing lens with a focal length of 50 mm and a silicon plane window mirror. As for the procedure followed to locate the 0°incident position, a similar approach to that employed in the 532 nm wavelength was used, although the details are not described here.

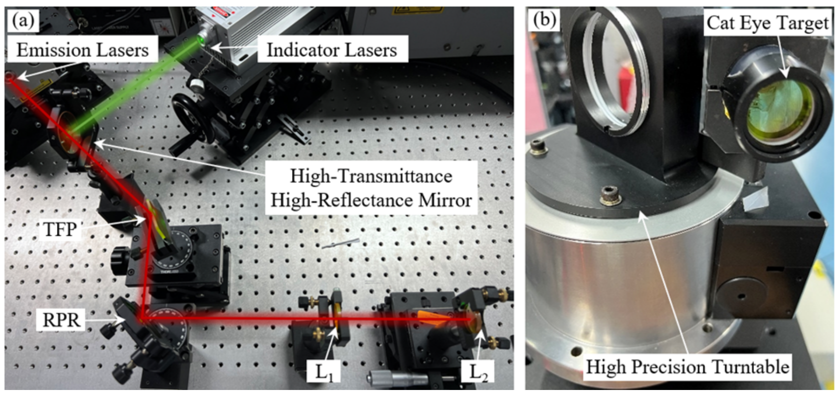


**Fig. 6.** (a) Physical image of the optical path of the transmitter and receiver for detecting the cat-eye target echo light field in the 10.6 um wavelength. (b) Physical image of cat-eye target in the 10.6 um wavelength and high precision turntable.

## 4. Analysis of experimental and simulation results

The formula (10) comprehensively describes the specific distribution of the 3D cat-eye target echo optical field for various wavelengths, incident angles, and defocusing levels. Numerical calculations used the same parameter values as the experimental conditions, and the peak intensity of the incident beam waist considered 1, with the simulation results reported as relative light intensity. During the experiment, echo power was measured and an image of the echo light spot obtained. Extracted and compared, the echo spot's centroid position, deflection, and diameter were discussed alongside the theoretical simulation results.

### *4.1. Impact of laser band on the echo optical field distribution*

The transmittance and reflectance parameters of different experimental equipment in the two band experiments are shown in Table 2. During the experiment, in order to avoid experimental errors caused by different equipment parameters in the two bands, we control that the output power after passing through the transmission system is the same.

Fitting curves for the emission power and the echo power of 532 nm and 10.6 um wavelengths were obtained in the experiment, with slopes of 0.04466 and 0.02386, respectively, as shown in Figs. 7(a) and (c). However, significant errors were found during the process of fitting the straight line. The main sources of analysis errors include poor stability of the emission light source and errors introduced by the measurement of the echo power meter. Comparison reveals that for zero defocusing, normal incidence, and equal emitter power and detection distance, the longer wavelength has a lower echo power than the shorter wavelength. Figures 7(b) and (d) depict theoretical simulation images of the echo spot distribution for the cat-eye target at 532 nm and 10.6 um, respectively. These images indicate that under the same conditions, center energy gradually spreads outward, peak energy reduces, and the echo spot diameter increases as incident

Optics EXPRESS

**Table 2. Parameters of different experimental device in the two band experiments**

| Visible laser band experimental device | Transmittance or Reflectivity | Far-infrared laser band experimental device | Transmittance or Reflectivity |
|---|---|---|---|
| OP | Transmittance 95.84% | HTHRM | Transmittance 99.13% |
| PBS | Transmittance 85.00% | TFP | Reflectivity 86.43% |
| QWP | Transmittance 87.34% | RPR | Reflectivity 86.74% |
| $L_1$ | Transmittance 98.22% | $L_1$ | Transmittance 98.97% |
| $L_2$ | Transmittance 99.76% | $L_2$ | Transmittance 99.23% |
| Cat-eye target lens | Transmittance 98.22% | Cat-eye target lens | Transmittance 98.97% |
| Silicon window mirror | Reflectivity 35.20% | Silicon window mirror | Reflectivity 37.08% |

wavelength increases. Hence, longer wavelengths have smaller echo power compared to shorter wavelengths, which is consistent with experimental results.

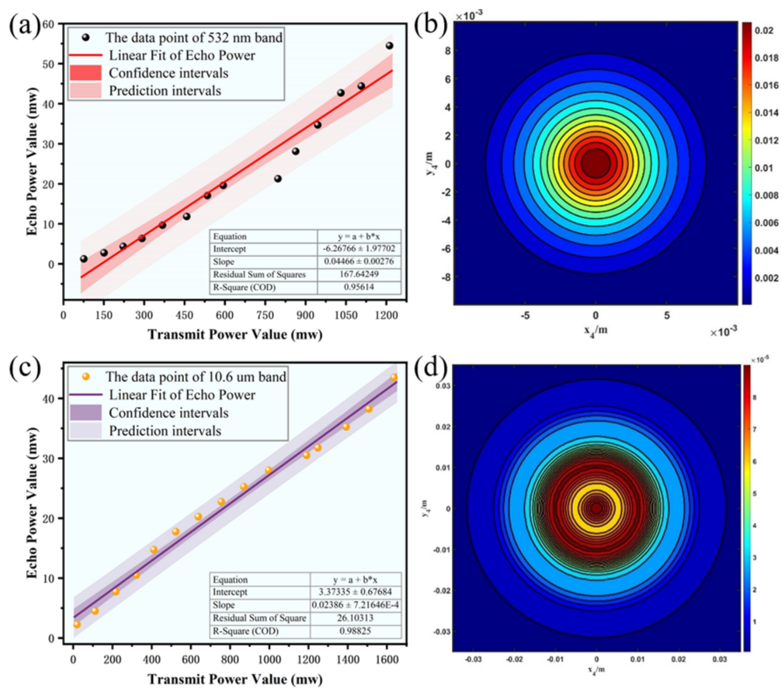


**Fig. 7.** (a),(c) Experimental fitting curves of transmission power and echo power. (b),(d) Theoretical simulation of the distribution of cat-eye target echo spot.

When the detection laser enters the cat's eye lens and converges to the focal plane, the reflected light starts from a small bright spot at the focal plane and returns in the original way. At this time, the bright spot is assumed to be a point light source, and the Airy disk formula is used for transmitting the reflected light to the echo detector. The diffraction-limited Airy disk diameter formula is given by Eq. (11), where $D_A$ is the diameter of the Airy disk and $D_H$ is the effective diffraction aperture of the cat-eye target. Because the actual echo may not necessarily fill the cat-eye target lens, the effective diffraction aperture of the cat-eye target is used for calculation. As per this formula, both the diffraction limit and the Airy disk diameter increase with the wavelength $\lambda$. As a result, during the detection of a cat-eye target, a higher incident light wavelength leads to a stronger diffraction effect. This effect causes the diameter of the echo light area to increase, the

Optics EXPRESS

energy of the echo to spread gradually, and the peak intensity to decrease. Ultimately, this leads to a reduction in the long-wavelength echo power compared to the short-wavelength power. This consistency between the experimental and theoretical results indicates the validity of both the experiments and the theoretical simulations.

$$D_A = 2.44 \cdot \frac{\lambda}{D_H} \cdot (L + f). \tag{13}$$

Applying the correlation between the wavelength of incident light and the echo power, information regarding the working band of a cat-eye target can be effectively obtained by analyzing the distribution of the echo light field through multi-band detection once the detection distance is determined. In subsequent studies, the diffraction effect in the echo spot was observed by changing the size of the emitted beam, in order to further elucidate the influence of wavelength on the echo spot.

### 4.2. Impact of defocus amount on the echo optical field distribution

In the experiment, the cat-eye target's silicon window mirror was placed on the displacement motor to conduct variable defocus experiments, and the brightest and smallest point after the lens was found and recorded as the focal point. In the two wavelength band experiments, the motor was used to drive the silicon window mirror to move forward and backward in 0.1 mm intervals, each time moving by 1 mm in front of and behind the focus. During this process, the echo power was measured and recorded each time, and multiple echo spot images were collected and the radius of each echo spot was extracted. The defocusing amounts used in the theoretical simulation were the same as those used in the experiment.

Figure 8 shows experimental and theoretical simulation images of the echo spot collected in the 532 nm wavelength under different positive and negative defocus values. Two changes to the echo spot occur with the introduction of defocus values: an increase in spot diameter and a decrease in both the spot's peak intensity and echo power. However, positive and negative defocus values of equal numerical value cause an asymmetrical change to the spot. In the experimental images, spots with equal numerical value of positive defocus have a higher peak intensity and echo power than their negative defocus counterparts. On the other hand, in the theoretical simulation images, spots with equal numerical value of positive defocus have a smaller diameter than their negative defocus counterparts.

Figure 9 shows the experimental and theoretical simulation images of the cat-eye target echo spot at 10.6 um for different positive and negative defocus amounts. Analyzing the experimental and theoretical simulation echo spot in the long-wave band yields the same experimental phenomenon as in the 532 nm wavelength: introducing the defocus variable causes the diameter, peak intensity, and echo power of the echo spot to change, and the impact of positive and negative defocus on the spot is asymmetric, with positive defocus having a smaller impact on the spot than negative defocus at the same numerical value. Conducting experiments in both the 532 nm and 10.6 um wavelengths confirms the presence of this phenomenon, demonstrating the scientific validity of the defocus amount proposed in this paper for the impact on the echo spot. However, through analyzing specific echo power and spot diameter data in both bands, it was found that a weak positive defocus amount resulted in the maximum echo power and minimum echo spot diameter, and that the numerical value of this minimum and maximum corresponded to the incident wavelength. This phenomenon will be detailed in the following section.

Data on the power and radius of the echo spot were plotted in Fig. 10 for two wavelength bands. Figures 10(a) and (c) show the defocusing and echo power data curves of the 532 nm and 10.6 um wavelengths, respectively. Figures 10(b) and (d) illustrate the defocusing and echo spot radius data curves of the 532 nm and 10.6 um wavelengths, respectively. By comparing the data curves from the experiments, we found that in the 532 nm, the echo spot radius reached a minimum

Optics EXPRESS

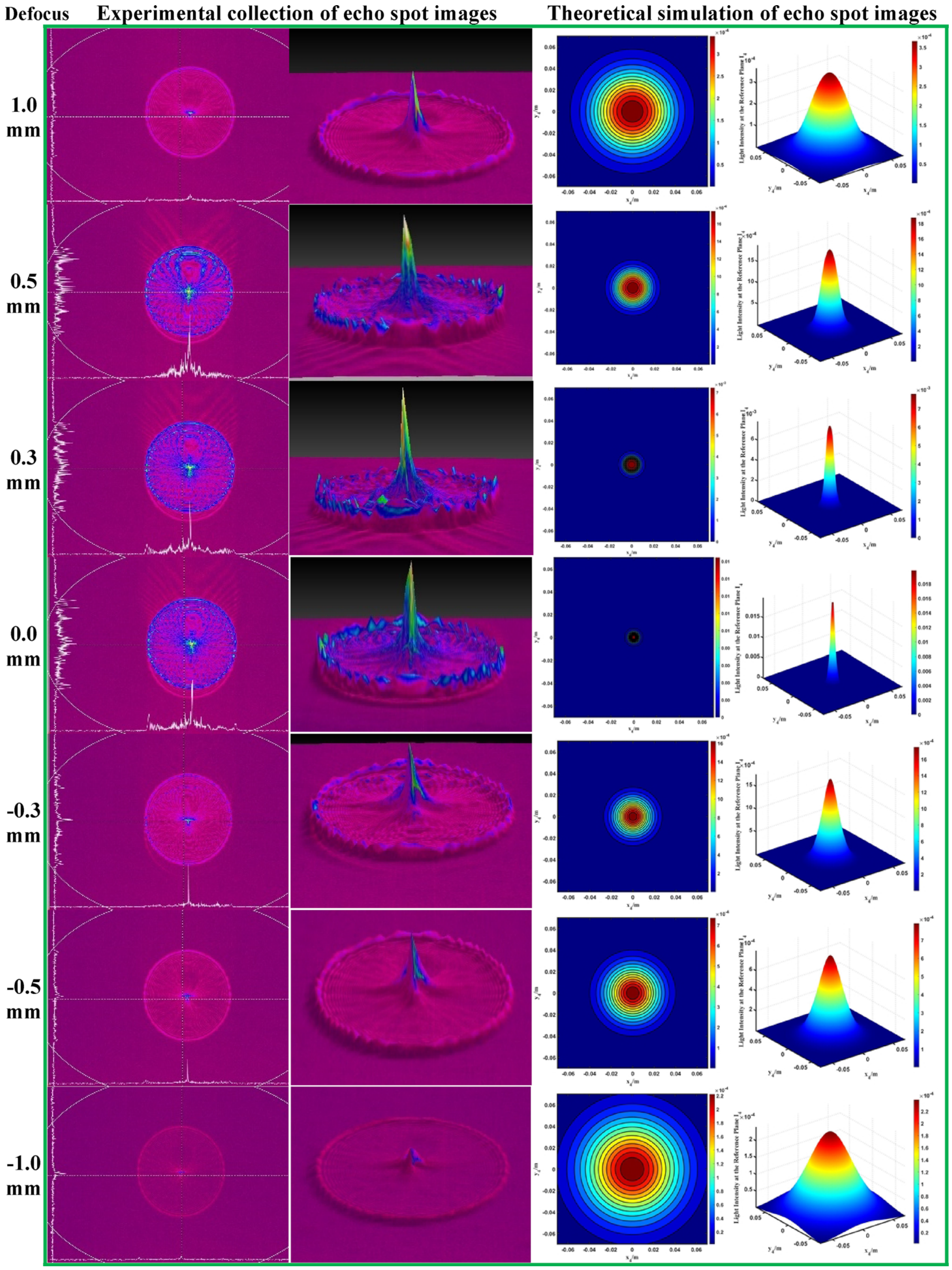


**Fig. 8.** Experimental echo spot images and theoretical simulation echo spot images of cat-eye targets collected at 532 nm under different positive and negative defocusing amounts.

and the echo power reached a maximum at a positive defocusing of 0.3 mm. In the 10.6 um, the echo spot radius reached a minimum and the echo power reached a maximum at a positive defocusing of 0.2 mm. In both experiments with two wavelengths, a phenomenon was observed in which the echo spot radius reached a minimum and the echo power reached a maximum at

Optics EXPRESS

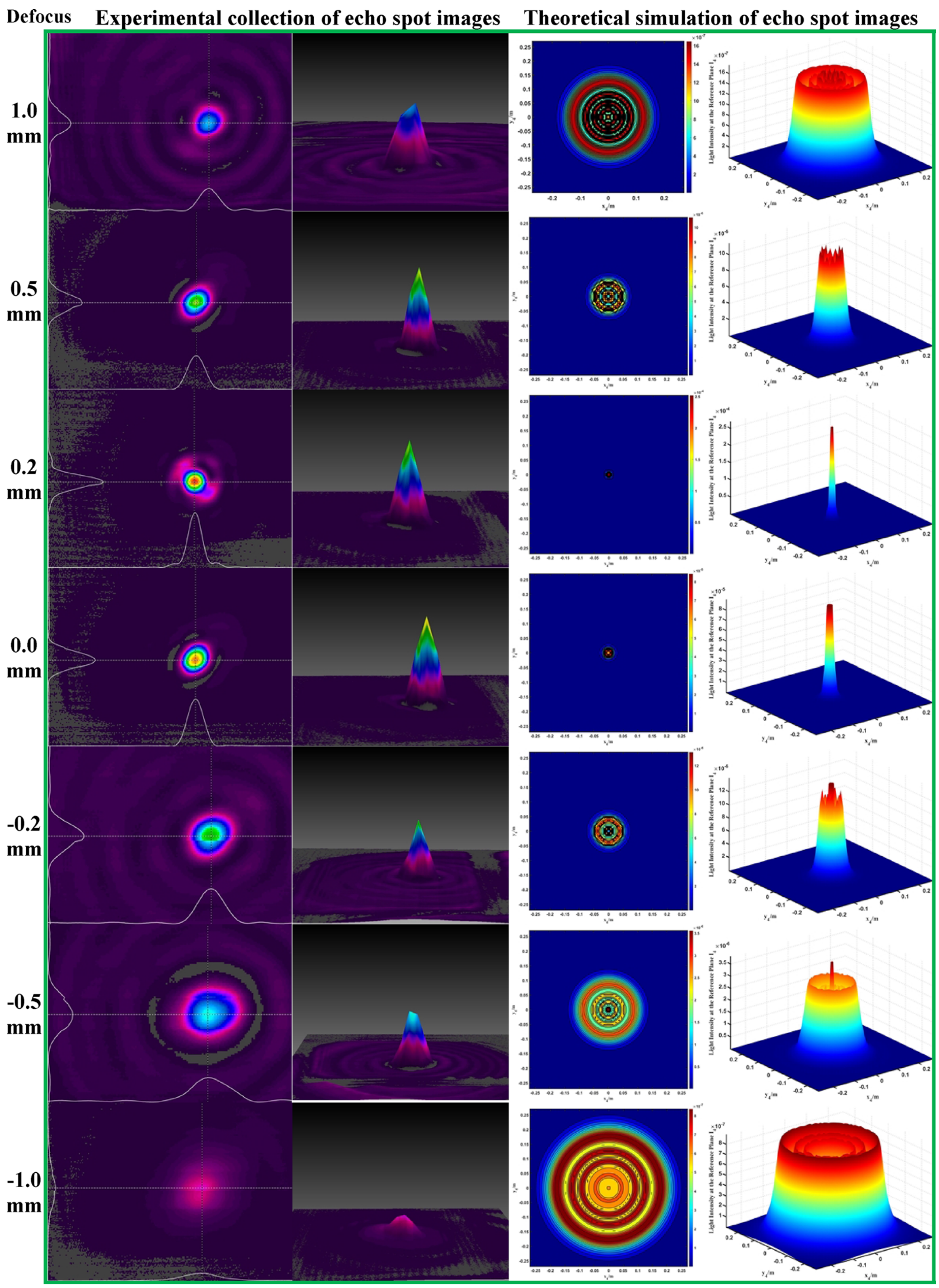


**Fig. 9.** Experimental echo spot images and theoretical simulation echo spot images of cat-eye targets collected at 10.6 um under different positive and negative defocusing amounts.

slight positive defocusing. Moreover, the values of slight positive defocusing that correspond to the phenomenon are different for the two wavelengths.

Optics EXPRESS

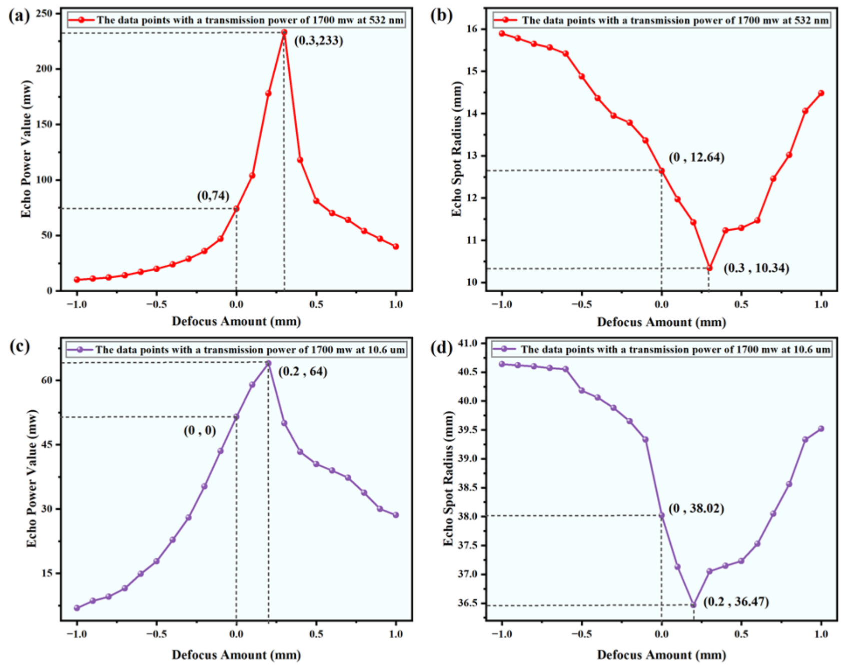


**Fig. 10.** (a) Experimental curves of defocus amount and echo power in the 532 nm. (b) Experimental curves of defocus amount and echo spot radius in the 532 nm. (c) Experimental curves of defocus amount and echo power in the 10.6 um. (d) Experimental curves of defocus amount and echo spot radius in the 10.6 um.

Data on the peak intensity, radius, and power of the echo spot were plotted in Fig. 11 for two wavelength bands in the theoretical simulation. Figures 11(a) and (d) show the curves of defocusing and peak intensity of the echo spot for the 532 nm and 10.6 um wavelengths, respectively. Figures 11(a) and (d) respectively indicate that when the defocus value is large, the echo power will decrease to a very low level, indicating that large defocus values should be avoided in practical use. Figures 11(b) and (e) show the curves of defocusing and radius of the echo spot for the 532 nm and 10.6 um wavelengths in the theoretical simulation, respectively. Figures 11(c) and (f) show the curves of defocusing and power of the echo spot for the 532 nm and 10.6 um wavelengths in the theoretical simulation, respectively. By comparing the curves in the theoretical simulation, we found that at a positive defocusing of 0.2 mm in the 532 nm and 0.1 mm in the 10.6 um, the echo spot radius reached its minimum and the echo power reached its maximum. The power of the echo spot reached the maximum when the intensity of the light per unit area was also at the maximum. The values of slight positive defocusing that correspond to the minimum echo spot radius and the maximum echo power in the theoretical simulation were 0.1 mm greater than the values in the actual experiments due to the inaccuracy in adjusting the defocusing caused by the insufficient precision of the displacement platform. However, the trend of defocusing affecting the echo spot was consistent with the actual experiments, both demonstrating the phenomenon in which the echo spot radius reached the minimum and the echo power reached the maximum at slight positive defocusing. Additionally, the values of slight positive defocusing were different for the two wavelengths.

In order to analyze this pattern and its causes, this paper considers the echo beam as a spherical wave emitted by a cat-eye target. As shown in Fig. 1, when the incident ray converges to a point on the focal plane of lens 1, all the rays in front of lens 2 can be regarded as a spherical wave emitted from that point. According to the theory of spherical wave transmission through a thin

Optics EXPRESS

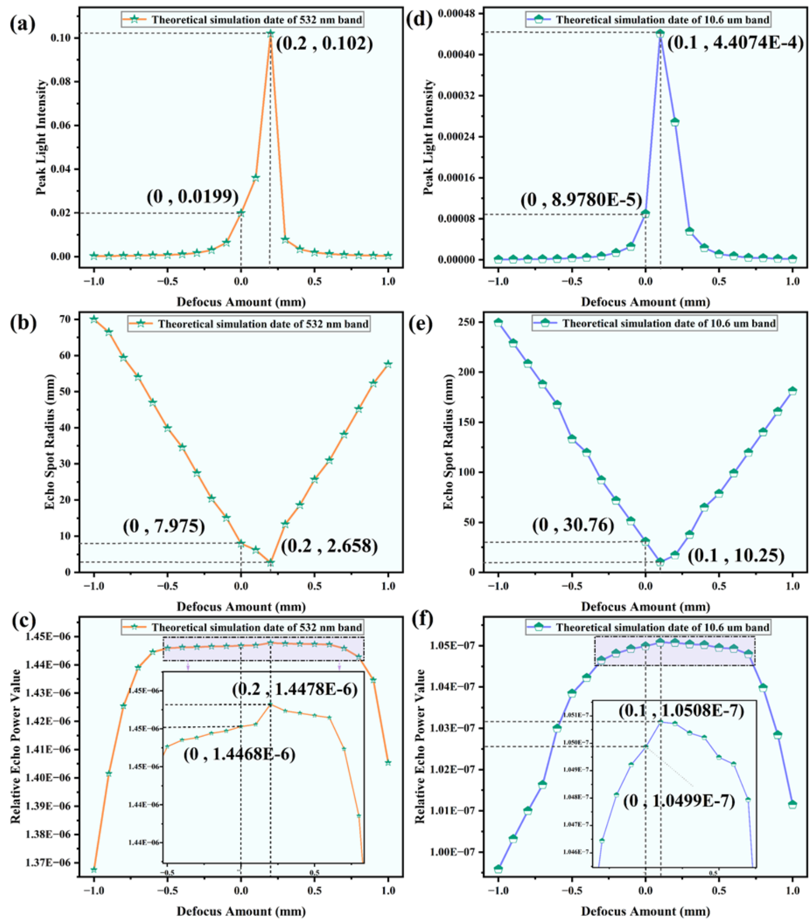


**Fig. 11.** (a),(d) Theoretical simulation diagram of defocus amount and echo peak light intensity in the 532 nm and 10.6 um. (b),(e) Theoretical simulation diagram of defocus amount and echo spot radius in the 532 nm and 10.6 um. (c),(f) Theoretical simulation diagram of defocus amount and relative echo power value in the 532 nm and 10.6 um.

lens, the reflected light behind lens 2 is still a spherical wave, which must have a convergence point, namely the center of the spherical wave. Assuming that the distance from the center of the spherical wave to the cat-eye target is $z_0$, it is defined as positive if the center and the receiving point are on the same side of the cat-eye target, and negative otherwise. According to the relationship between the object and image, the values of $z_0$ in over-focusing and under-focusing situations can be written as follows:

$$z_{0+} = \frac{f(f+2\delta)}{2\delta}, z_{0-} = \frac{f(f-2\delta)}{2\delta}. \tag{14}$$

Formula (12) shows that when there is no defocus, the center of the echo beam is at infinity, that is, it behaves like ideal parallel light. In defocus situations, the echo beam of cat-eye effect can be equivalent to a conical spherical wave emitted from the cat-eye target. In under-focusing, the center of the spherical wave is on the opposite side of the target than the receiving point. As the defocus increases, the cone angle of this spherical wave gradually increases, causing the distribution of the echo at the receiving end to increase gradually. This corresponds to the fact that the radius of the echo spot increases continuously in both experimental and theoretical

Optics EXPRESS

under-focusing situations, causing the power of the echo at the receiving end to gradually decrease. In over-focusing, the center of the equivalent spherical wave is on the same side of the target as the receiving point. As the defocus increases, the center of the spherical wave moves gradually towards the target, and the cone angle gradually increases. However, when there is a slight positive defocus, the center of the spherical wave is farther away from the receiving end than the detection distance, and the area of the distribution of the spherical wave at the receiving end decreases as the defocus increases, resulting in an increase in the power of the echo at the receiving end. When the positive defocus is larger and the center of the spherical wave is closer to the target than the detection distance, the power of the echo at the receiving end decreases as the defocus increases. This phenomenon is consistent with the research results of the three interval theoretical mode of the Ref. [18], which were verified by both theoretical simulations and experiments in this study. It was further suggested that the value of the weak positive defocus when this phenomenon occurs is related to the wavelength of the incident light.

### *4.3. Impact of laser incident angle on the echo optical field distribution*

To conduct the variable angle of incidence experiment, cat-eye targets in different wavelengths were placed on a high-precision turntable in Figs. 4(b) and 6(b), respectively. The reflector formed a circular spot and the echo power reached the maximum value when the incidence angle was set to 0° through micro-adjustment of the turntable angle. The cat-eye target was driven by the high-precision turntable, with 0.5° intervals from -4° to 4° in both experiments. During this process, the echo power was measured and recorded after each rotation, and multiple frames of echo spot images were captured to extract the average centroid position of each echo spot, and thereby calculate the defocus value of the echo spot. Theoretical simulations of the two wavelengths were also conducted at intervals of 0.5° from -4° to 4° to obtain the simulated echo spot images, from which the centroid position of each simulated echo spot was extracted.

The experiment images and theoretical simulations of the target cat-eye reflection in the 532 nm wavelength at different laser incidence angles are presented in Fig. 12. The comparison between the theoretical simulation and experimental collected images for the 532 nm wavelength clearly indicates two changes in the reflection when the incidence angle is altered: Firstly, the entire position of the reflection shifts along with the centroid of the reflection. Secondly, the peak intensity and the power of the reflection reduces. These changes are consistent with the impact of the incidence angle change at 10.6 um, which is why it is not presented explicitly.

The collected experimental and simulated data for two wavelengths on the power and incidence angle of the reflection are presented in Fig. 13. Figures 13(a) and (c) show the experimental data curve of the incidence angle and the reflection power for the 532 nm and 10.6 μm, while Figs. 13(b) and (d) show the corresponding theoretical simulation curves for these parameters. By comparing the scaled graph in Figs. 13(a) and (c) with the curves in the main diagram, it is found that the pattern of echo power decreasing with decreasing angle is the same under different transmission power conditions. An analysis of Figs. 13(a) and (c) revealed that, for different wavelengths and powers, the reflection power gradually reduces as the laser incidence angle increases. After the incidence angle exceeds 4°, the reflection power drops to a low level. This corresponds to the conclusion obtained in the three interval model that as the angle increases, the echo intensity gradually decreases. By comparing the horizontal axes of Figs. 13(a) and (b) as well as Figs. 13(c) and (d), it is evident that the influence of laser incidence angle on the reflection power is consistent between the theoretical simulations and experimental results for both wavelengths.

To further analyze the effect of incidence angle variation on the reflection spot, we define the centroid coordinates and the spot displacement quantity. These definitions enable quantitative processing of the reflection spot images. The centroid coordinates of the reflection spot are determined by the first moment of the spot data. The absolute difference between the centroid of

Optics EXPRESS

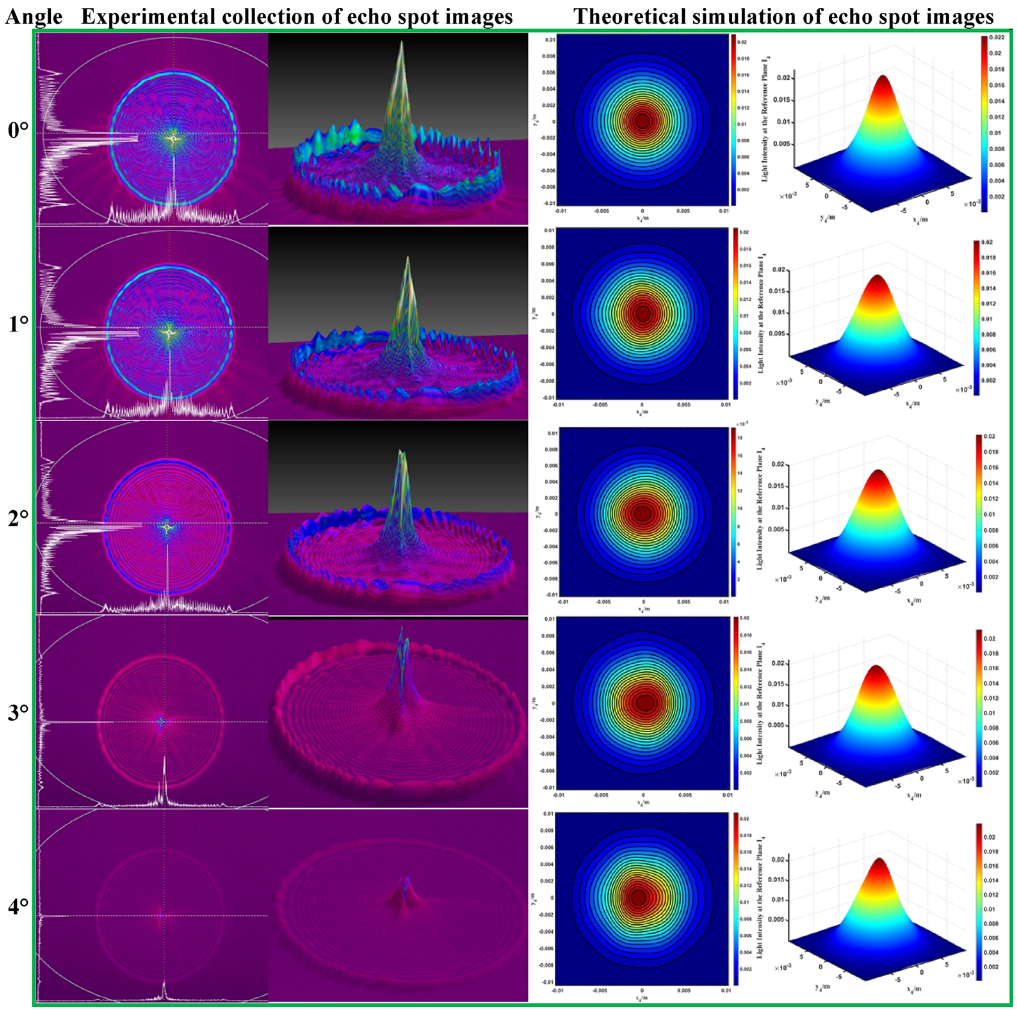


**Fig. 12.** Experimental echo spot images and theoretical simulation echo spot images of cat-eye targets collected at 532 nm under different laser incident angle.

the reflection spot at different incidence angles and the centroid at zero incidence angle is defined as the spot displacement quantity. The equation can be written as follows:

$$\begin{gathered} x(k)=\frac{\sum_{j=1}^{m}\sum_{i=1}^{n}x_{ij}I_{ij}(k)}{\sum_{j=1}^{m}\sum_{i=1}^{n}I_{ij}(k)}\quad y(k)=\frac{\sum_{j=1}^{m}\sum_{i=1}^{n}y_{ij}I_{ij}(k)}{\sum_{j=1}^{m}\sum_{i=1}^{n}I_{ij}(k)} \\ \Delta x(k)=|x_0(k)-x_\theta(k)|\Delta y(k)=|y_0(k)-y_\theta(k)|, \end{gathered} \tag{15}$$

where $x(k)$ and $y(k)$ are the transverse and longitudinal coordinates of the spot centroid, respectively, n and m are the number of pixels in the $x$ and $y$ directions of the receiving plane, respectively, $x_{ij}$ and $y_{ij}$ are the $x$- and $y$-coordinate values corresponding to the number of pixels in the receiving plane, respectively, $I_{ij}(k)$ are the light intensity values corresponding to the pixels, $y_0$(k) and $y_\theta(k)$ are the ordinate of the spot centroid corresponding to 0° and θ° incident angles, respectively, and $\Delta x(k)$ and $\Delta y(k)$ are the target-missing quantities in the $x$ and $y$ directions, respectively. This study only considers incidence at different angles in the $x$ direction, and the $y$ direction is similar.

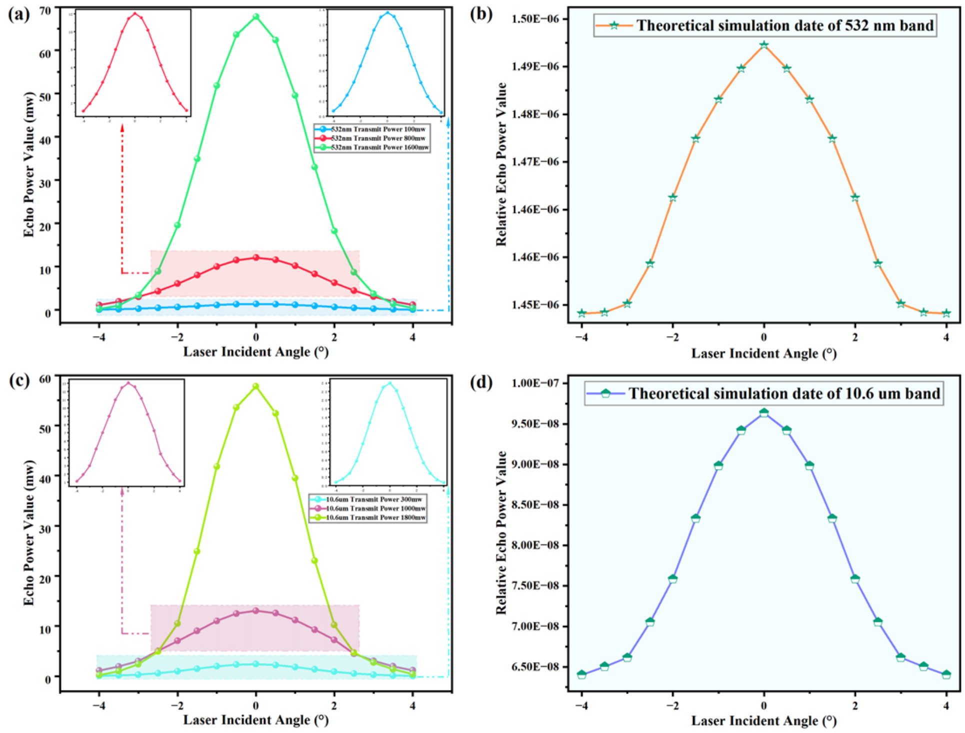


**Fig. 13.** (a) Experimental curves of laser incident angle and echo power in the 532 nm. (b) Theoretical simulation diagram of laser incident angle and echo power in the 532 nm. (c) Experimental curves of laser incident angle and echo power in the 10.6 um. (d) Theoretical simulation diagram of laser incident angle and echo power in the 10.6 um.

Figure 14 shows the centroid coordinates and miss distance data of the echo spot in both experimental and theoretical simulations collected from two spectral bands. Figures 14(a) and (d) display the box plot of the experimental data of the centroid coordinates of the echo spot in the 532 nm and 10.6 um, respectively, as a function of the angle of incidence. This box diagram can observe the overall concentrated distribution of echo spot data. The overall size of the box in the figure is relatively small, indicating that the experimental data distribution is relatively concentrated and the error is small. Figures 14(b) and (e) plot the experimental data of the target-missing quantities of the echo spot as a function of the angle of incidence in the 532 nm and 10.6 um, respectively, by the curve fitting. Figures 14(c) and (f) show the theoretical results of the target-missing quantities of the echo spot as a function of the angle of incidence in the 532 nm and 10.6 um, respectively. By analyzing Figs. 14(b) and (e), it is observed that the target-missing quantities of the echo spot has a linear relationship with the angle of incidence in the experimental setup of different incident wavebands. Similarly, the analysis of Figs. 14(c) and (f) demonstrates that in theoretical simulations of different incident wavebands, the target-missing quantities of the echo spot also exhibits a linear relationship with the angle of incidence, which is in good agreement with the experimental results, demonstrating the scientific and rational nature of the proposed theory and experimental conclusions. The discovered linear relationship can provide a theoretical basis for trajectory prediction to achieve real-time tracking and active detection of moving cat-eye targets. We will use the field of view of the cat's eye target and the influence of vignetting on the echo spot as our future research plan.

Optics EXPRESS

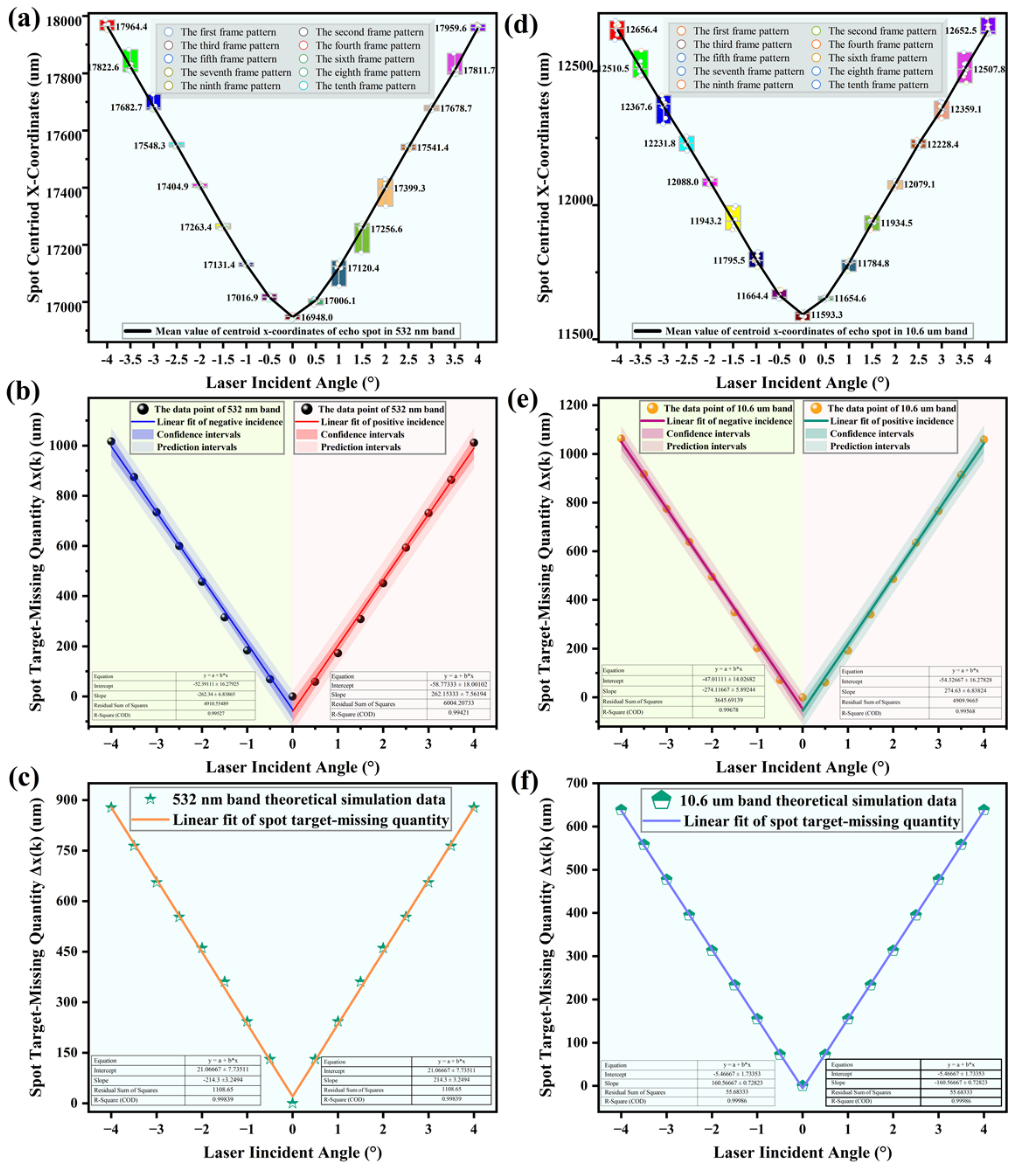

**Fig. 14.** (a),(d) Experimental box diagram of laser incident angle and spot centroid *x*-coordinates in the 532 nm and 10.6 um. (b),(e) Experimental fitting curves of incident angle and spot target-missing quantity in the 532 nm and 10.6 um. (c),(f) Theoretical simulation diagram of incident angle and spot target-missing quantity in the 532 nm and 10.6 um.

## 5. Conclusion

In summary, this study addresses the lack of quantitative analysis of variable factors, such as incident wavelength and defocus, in laser active detection based on the cat-eye effect. The study proposes a four-interval theoretical model for detecting dual-band cat-eye targets by combining matrix optical theory and Collins diffraction integration in theoretical research. The method overcomes the problem of the inapplicability of the Collins diffraction formula under large-angle incident conditions using a coordinate system rotation method. The study conducts dual-band echo detection using 10.6 um far-infrared and 532 nm visible light in experiments, solving the problem of insufficient research on the influence of incident wavelength in cat-eye effect research. By collecting theoretical and experimental data on echo power, echo spot radius, echo spot centroid coordinates, and centroid defocus, the study quantitatively analyzes the impact of incident wavelength, defocus, and angle variables on echo spot.

The research results show that the detection light band affects the echo field distribution by changing the diffraction limit, and under the same other variables, the echo power of far-infrared detection light is lower than that of visible light. The defocus variable changes the radius, peak intensity, and power of the echo spot, and the asymmetrical spot change introduced by positive and negative defocusing is different. Under the same numerical value, positive defocusing has less impact on the spot than negative defocusing. When there is a weak positive defocus, the echo spot radius reaches its minimum, and the echo power reaches its maximum. Moreover, the numerical value of the weak positive defocus corresponding to different detection bands varies. The incident angle variable of the detection laser changes the echo spot centroid coordinates and echo power. After introducing the definition of echo spot target-missing quantities, the incident angle of the laser and the target-missing quantities of the echo spot demonstrate a linear relationship. The theoretical and experimental conclusions proposed in this paper can effectively obtain the working waveband information of cat-eye targets by analyzing the distribution of echo light fields during multi-band detection, providing a theoretical basis for predicting trajectories and achieving real-time continuous tracking and detection of high-speed moving cat-eye targets. However, the cat-eye target is composed of a focusing lens and a plane mirror in this model, but the real cat's eye target is not made up of this. This article lacks research on the impact of detection distance variables on echo detection. In the future work, we will use the actual CCD instead of the simple cat's-eye target model under the case of remote detection. And the influence of atmospheric turbulence on light wave propagation will be considered.

**Funding.** Funding of 'Xuguang Talents' from CIOMP; Innovation Cross team of the Chinese Academy of Sciences; Youth Innovation Promotion Association of the Chinese Academy of Sciences; National Natural Science Foundation of China.

**Disclosures.** The authors declare no conflicts of interest.

**Data availability.** Data underlying the results presented in this paper may be available from the corresponding author upon reasonable request.

## References

1. M. Gong and S. F. He, "Periodicity analysis on cat-eye reflected beam profiles of optical detectors," Opt. Eng **56**(5), 053110 (2017).
2. Y. Z. Zhao, H. Y. Sun, Y. H. Zheng, C. M. Shan, and Y. C. Fan, "An interferometry measure method on vibration spectrum of optical target based on cat-eye effect," Opt. Laser Technol. **58**, 1–7 (2014).
3. M. Portnoi, P. A. Haigh, T. J. Macdonald, F. Ambroz, I. P. Parkin, I. Darwazeh, and I. Papakonstantinou, "Bandwidth limits of luminescent solar concentrators as detectors in free-space optical communication systems," Light: Sci. Appl. **10**(1), 3 (2021).
4. T Liu, M Rajadhyaksha, and D L. Dickensheets, "MEMS-in-the-lens architecture for a miniature high-NA laser scanning microscope," Light: Sci. Appl. **8**(1), 59 (2019).
5. Z. B. Fan, H. Y. Qiu, H. L. Zhang, X. N. Pang, L. D. Zhou, L. Liu, H. Ren, Q. H. Wang, and J. W. Dong, "A broadband achromatic metalens array for integral imaging in the visible," Light: Sci. Appl. **8**(1), 67 (2019).
6. Z. Z. Cao, X. B. Zhang, G. Osnabrugge, J. H. Li, and I. M. Vellekoop, and A. M. J. Koonen, "Reconfigurable beam system for non-line-of-sight free-space optical communication," Light: Sci. Appl. **8**(1), 69 (2019).
7. Y. Z. Zhao, H. Y. Sun, and L. X. Zhang, and Y. H. Zheng, "Light intensity at the return place and encirclement power ratio for the distorted reflected beam based on cat-eye effect," J," Optoelectron. Lett. **7**(6), 478–482 (2011).
8. Y C Li, Z F Hou, and Y C. Fan, "The simulation study on optical target laser active detection performance," *C. International Symposium on Optoelectronic Technology & Application: Laser & Optical Measurement Technology & Fiber Optic Sensors. International Society for Optics and Photonics.* (2014).
9. S F. He, M. Yuan, and M. Gong, "Active laser detection system for recognizing surveillance devices," Opt. Commun. **426**, 313–324 (2018).
10. S. F. He, M. Yuan, and M. Gong, "Freeform lens design to eliminate retroreflection for optical systems," Appl. Opt. **57**(5), 1218–1224 (2018).

Optics EXPRESS

11. Z. Lv, X. C. Du, K. Zhang, and F. Chen, "Three-dimensional echo distribution analysis of multi-band and oblique Gaussian beams propagating through cat-eye optical system," Opt. Laser Technol. **151**, 108044 (2022).
12. X. Wang, H. Chen, Y. Tian, and B. Qu H, "Real-time quality control of dripping pill's weight based on laser detection technology," Sci. Rep. **13**(1), 6153 (2023).
13. N. A. Macleod, F. Molero, and D. Weidmann, "Broadband standoff detection of large molecules by mid-infrared active coherent laser spectrometry," Opt. Express **23**(2), 912–928 (2015).
14. F. Fuchs, S. Hugger, M. Kinzer, R. Aidam, W. Bronner, R. Losch, Q. K. Yang, K. Degreif, and F. Schnurer, "Imaging standoff detection of explosives using widely tunable midinfrared quantum cascade lasers," Opt. Eng **49**(11), 111127 (2010).
15. D S. Wu, B Q. Liu, W G. Hu, J. Liu, and J J. Ying, "Echo characteristic model of cat-eye effect based on matrix optics," J. Journal of Optics. **36**, 0608001 (2016).
16. B Q. Liu, B. Zhou, D S. Wu, and Y. Zhang, "Dual-channel active laser detection system," J. Optics and Precision Engineering. **20**, 241–246 (2012).
17. Y Z. Zhao, H Y. Sun, and Y H. Zheng, "An approximate analytical propagation formula for Gaussian beams through a cat-eye optical lens under large incidence angle condition," Chinese Phys. Lett. **28**(7), 074101 (2011).
18. M X. Zhang, Y. Lv, X Y. Li, R. Geng, and G L. Sheng, "Theoretical analysis on retro-reflected wave power based on "cat-eye" effect in defocusing condition," Appl. Mech. Mater. **644-650**, 1342–1345 (2014).